Arch. Metall. Mater. **67** (2022), 3, 913-920

DOI: https://doi.org/10.24425/amm.2022.139683

ZHALE NAZARI[1], DAVOD SEIFZADEH[1*], ZAHRA RAJABALIZADEH[1]

ELECTROLESS NICKEL PLATING ON AM60B MAGNESIUM ALLOY VIA Ti-Zr/SOL-GEL COMPOSITE LAYER AS PRETREATMENT

The Ti-Zr and Ti-Zr/sol-gel were used as pretreatment layers before the electroless nickel coating on AM60B magnesium alloy. Scanning Electron Microscopy was employed to investigate the surface morphology of the pretreated layers and applied electroless coatings. Chemical analysis of the Ti-Zr layer, and nickel coatings was done using the Energy-Dispersive X-ray Spectroscopy. Moreover, the X-ray Diffraction and Atomic Force Microscopy methods were utilized to evaluate the microstructure and surface roughness of the electroless coatings, respectively. Electrochemical Impedance Spectroscopy was employed to study the corrosion behavior of Ni-P coatings. The results show that Ti-Zr layer has structural cracks, and the sol-gel film was covered all cracks entirely. The cauliflower-like electroless nickel coating was applied on both mentioned pretreated layers. The cross-sectional images revealed the higher thickness for the electroless coating on Ti-Zr/sol-gel layer, probably due to a large number of Ni nucleation centers. The EIS results demonstrate that the electroless coating on Ti-Zr/sol-gel has high corrosion protection and microhardness value.

Keywords: Sol-gel; Mg alloy; Electroless plating

1. Introduction

Recently, Mg has been introduced as the lightest and most commonly used metal, which unfortunately encounters problems such as poor wear and corrosion resistance [1-3]. Electroless Ni-P plating has been considered as a practical approach to overcome this problem and improve the corrosion resistance [4,5]. However, applying the electroless nickel coating on Mg is faced with difficulties due to some reasons. The first one is the relatively high corrosion rate of magnesium especially in aqueous environment due to the high electrochemical reactivity. Besides, electrochemical heterogeneity of the magnesium alloys and the existence of natural porous and non-adhesive oxide/hydroxide layer make the plating so difficult [6,7]. Traditionally, chromium conversion layer was introduced as a pretreatment before the electroless coating to overcome these problems. In order to homogenize the alloy surface and remove the loose oxide/hydroxide layer, the magnesium alloy was immersed in CrO_3+HNO_3 solution before the electroless plating [8,9]. However, toxicity of the chromium compounds has persuaded the researchers to suggest several environmentally-friendly conversion coatings [10-12]. Despite the desirable results, the main drawback of these pretreatment layers is that the obtained nickel coating should be pore-free. In the porous nickel coatings, the corrosive solution will penetrate through the grain boundaries and the conversion layer cannot protect the substrate due to its inherent porosities and therefore, the galvanic corrosion will destroy the magnesium substrate [13-15]. Development of silica layer by the sol-gel method as a pretreatment layer before the electroless plating can be examined. Despite the many advantageous and relative resistance of the silica layer against the corrosive solution, application of the defect-free and high-quality sol-gel coating on the Mg alloy is still a challenge [16,17]. The defects of the sol-gel coating because of the reaction of magnesium substrate with the sol solution (with pH value between 1-1.5 due to the application of acidic catalysis) and hydrogen releases leads to the porous and cracky coating [18-20]. Recently, composite conversion coating/sol-gel layer was used as a corrosion protective coating on the magnesium alloys [21,22]. Conversion coatings have some advantages such as uniform deposition, low cost and excellent adhesion, but unfortunately, these coatings are porous, too. However, by applying the conversion layer as a primer for the sol-gel coating, the adhesion and corrosion resistance of the sol-gel coating increase because the inherent pores of the conversion layer seals by the silica film. In other words, by applying the composite conversion layer/sol-gel coating the corrosion

[1] UNIVERSITY OF MOHAGHEGH ARDABILI, FACULTY OF SCIENCE, CORROSION AND INDUSTRIAL ELECTROCHEMISTRY RESEARCH LABORATORY, ARDABIL-IRAN

* Corresponding author: seifzadeh@uma.ac.ir

© 2022. The Author(s). This is an open-access article distributed under the terms of the Creative Commons Attribution-NonCommercial License (CC BY-NC 4.0, https://creativecommons.org/licenses/by-nc/4.0/deed.en which permits the use, redistribution of the material in any medium or format, transforming and building upon the material, provided that the article is properly cited, the use is noncommercial, and no modifications or adaptations are made.

protection performance of the coating improves more than the pure sol-gel and conversion coating [22]. Murillo-Gutierrez et al. [23] studied the anticorrosion behavior of the phosphate-based conversion layer and hybrid sol-gel coating on a cast Elektron 21 magnesium alloy. They claimed that the applied sol-gel coating improved the corrosion performance of the Mg substrate significantly and also, the presence of an intermediate phosphate conversion layer caused more promotion of the corrosion resistance. Hu et al. [24] investigated the corrosion performance of AZ91D magnesium alloy by applying a molybdate base conversion coating/three layers of silicon sol-gel coatings. They reported that the corrosion resistance of the substrate was improved by the Mo conversion layer to some extent, but further improvement was obtained after the deposition of the sol-gel coating. Therefore, a composite conversion coating/sol-gel layer could be used as an environmentally-friendly replacement for the traditional chromate conversion layer. Moreover, this composite pretreatment layer has advantages for both the conversion coating and sol-gel layer. The use of composite conversion coating/sol-gel layer as a pretreatment before electroless coating has not been reported.

In this work, Ti-Zr/sol-gel coating was used as a pretreatment layer before the electroless Ni-P coating on AM60B magnesium alloy. The surface morphology of the pretreatment layers and electroless coatings was studied by Scanning Electron Microscopy (SEM). Moreover, the elemental analysis, microstructure, and topography of the obtained nickel coating were investigated by the Energy-Dispersive X-ray Spectroscopy (EDS), X-ray Diffraction (XRD) and Atomic Force Microscopy (AFM) methods, respectively. The Electrochemical Impedance Spectroscopy (EIS) tests were carried out to investigate the corrosion behavior of the coating. Also, the microhardness of the coatings was measured by Vickers hardness. All results were compared with the applied electroless Ni-P coating on the Ti-Zr conversion layer.

2. Experimental

2.1. Samples preparation process

2.1.1. Electroless Ni-P coating on Ti-Zr conversion layer

After abrading AM60B magnesium alloy surface with SiC paper, the specimens were immersed in acetone ultrasonically for 15 min at 45°C. Then the cleaned samples were transferred into the conversion bath containing 0.5 g/L H_2TiF_6 and 1.5 g/L H_2ZrF_6 with pH~2.5 (adjusted by adding NaOH solution dropwisely) for 8 min at 30°C. After that, the pretreated magnesium samples were immersed into the nickel plating bath (Table 1).

2.1.2. Electroless nickel coating on Ti-Zr/sol-gel

To prepare the sol solution, 0.02 mol tetraethylorthosilicate (TEOS) and 0.02 mol γ-glycidyloxypropyltrimethoxysilane (GPTMS) were mixed. After that, 0.3 mol acidic water (HCl with pH~1.5) was added to the prepared solution to start the hydrolysis process [26]. The sol solution was agitated using magnetic stirrer at room temperature for 2 h and then was remained without agitation for 24 h. The conversion-treated samples (in the above mentioned conversion bath) were immersed in the prepared sol-gel solution for 5 min using a dip-coater and withdrawn at 50 mm/min. To obtain the thick film, this process was repeated four times. To slow evaporation of the residual water, the sol-gel treated specimens were kept in a digital furnace for 2 h at 60°C and then heated at 130°C for 1 h. After that, the samples were immersed in a NaOH aqueous solution (200 g/L) at 50°C for 15 min for the surface roughing. Then, the sensitization was done in a solution containing HCl (20 ml/L) and $SnCl_2$ (10 g/L) for 5 s at 30°C which was followed by activation in the silver solution for 60 s. To prepare the activation solution, $AgNO_3$ (12 g/L) and of NaOH (10 g/L) were mixed and a solution with black color was obtained immediately. Afterwards, ammonia was added dropwise to the solution until it became clear. Finally, the activated samples were immersed in the electroless plating bath according to TABLE 1.

TABLE 1

Bath composition and operation condition of the electroless plating bath

Bath composition		Condition
$NiSO_4.6H_2O$ (Merck, 99%)	15 g L^{-1}	Temperature: 65°C
$NaH_2PO_2.H_2O$ (Loba chemie, 99%)	14 g L^{-1}	pH = 6.4
$NaC_2H_3O_2$ (Merck, >99.5%)	13 g L^{-1}	
NH_4HF_2 (Loba chemie, 98%)	8 g L^{-1}	
HF (Loba chemie, 40% v/v)	12 mL L^{-1}	
$CuSO_4$. $5H_2O$ (Merck, extra pure)	0.2 g L^{-1}	
NH_3 for pH adjusting (Rankem, 30%)	—	
Thiourea (Merck, extra pure)	1 ppm	

2.2. Coating characterization

Surface morphology of the prepared samples including Ti-Zr layer, electroless nickel coating on Ti-Zr layer, Ti-Zr/sol-gel coating and electroless nickel coating on Ti-Zr/sol-gel layer was done by SEM (LEO, VP 1430) instrument. The cross-section observations of the electrolessly plated coatings were also performed. Also, EDS (RÖNTEC GmbH Germany) method was employed for the elemental analysis of Ti-Zr layer and nickel coatings. For this purpose, the EDS analysis was applied from three different points of the surface, and the standard deviation of the data was reported, too. The microstructure of the applied electroless coatings was studied by the XRD analyzer (Phillips Xpert) with Cu kα radiation (λ = 0.154178 nm). The topographical images of the electrolessly plated coatings were obtained using the AFM device (Core AFM, Nanosurf) with Si_3N_4 cantilever tip and in non-contact mode.

2.3. Corrosion tests

The corrosion performance of the electroless coatings applied on the Ti-Zr and Ti-Zr/sol-gel pretreatment layers was investigated by the EIS method in NaCl (3.5 wt. %) as a corrosive solution. For this reason, μAutolab 3 Potentiostat/Galvanostat instrument and Nova 1.6.013 software along with the saturated Ag/AgCl and Pt sheet (1 cm^2) as reference and counter electrodes were utilized, respectively. Also, the Ni-P coated samples as working electrodes were masked in the epoxy resin before the corrosion tests and just 1 cm^2 of them were exposed to the corrosive solution. For the EIS tests, sine wave ac voltage with an amplitude of 10 mV and frequency range from 100000 to 0.01 Hz was applied. To reach the steady-state, all samples remained in the corrosive solution for 30 min and then the EIS tests were performed in the Open Circuit Potential (OCP).

2.4. Microhardness

The Vickers micro-hardness of Ni-P coated samples were measured according to the ASTM E384-16. The diamond indenter with a load of 25 g for 10 s was applied on the samples and the results of three different measurements were averaged.

3. Results and discussions

3.1. Ti-Zr and Ti-Zr/sol-gel pretreatment layers

Fig. 1 shows the surface morphology of Ti-Zr and Ti-Zr/sol-gel pretreatment layers on AM60B magnesium alloy. Fig. 1a represents that the surface of the substrate was entirely covered by cracked Ti-Zr conversion layer. Also, some bright zones were evident on the surface, probably attributing to the deposition of heavy atoms such as Ti and Zr [25]. The formation mechanism of the Ti-Zr layer can be described as follows [26,27]. After immersion of the alloy sample into the acidic conversion bath, the naturally formed oxide/hydroxide film removes due to the presence of fluorides and intermetallic phases are exposed to the conversion solution:

$$TiF_6^{2-} \rightarrow Ti^{4+} + 6F^- \quad (1)$$

$$ZrF_6^{2-} \rightarrow Zr^{4+} + 6F^- \quad (2)$$

The intermetallic phases on the substrate act as a driving force for the formation of conversion layer since each phase behaves differently. Cathodic reactions like oxygen reduction (in the presence of water) and hydrogen evolution take place on the β-phases and anodic reaction (magnesium dissolution) on the α-phases of the magnesium alloy:

$$Mg \rightarrow Mg^{2+} + 2\bar{e} \quad (3)$$

$$O_2 + 2H_2O + 4\bar{e} \rightarrow 4OH^- \quad (4)$$

$$2H^+ + 2\bar{e} \rightarrow H_2 \quad (5)$$

The induced alkalization around the cathodic sites causes to the precipitation of Ti and Zr containing oxide conversion film:

$$Mg^{2+} + 2OH^- \rightarrow Mg(OH)_2 \downarrow \quad (6)$$

$$Ti^{4+} + 4OH^- \rightarrow TiO_2 \downarrow + 2H_2O \quad (7)$$

$$Zr^{4+} + 4OH^- \rightarrow ZrO_2 \downarrow + 2H_2O \quad (8)$$

After initial local precipitation around the intermetallic phases, the deposition extends and covers the surface entirely. Longer immersion time, results to complete coverage and thickening of the film and finally crack structure. The presence of cracks on the surface could be attributed to the H_2 evolution during the formation steps and water removal in the drying process. The EDS results revealed that the conversion layer contains Mg (31.72 ±2.57 wt. %), O (13.74 ±8.14 wt. %), Ti (10.29 ±1.0 wt. %), Zr (39.25 ±5.62 wt. %), Al (1.85 ±0.54 wt. %), Mn (0.31 ±0.20 wt. %) and Zn (2.85 ±1.18 wt. %). The presence of Ti, Zr, and O agrees with the above-mentioned mechanism.

Fig. 1b represents the surface morphology of the Ti-Zr/sol-gel pretreatment layer. As is clear, the surface of the Ti-Zr

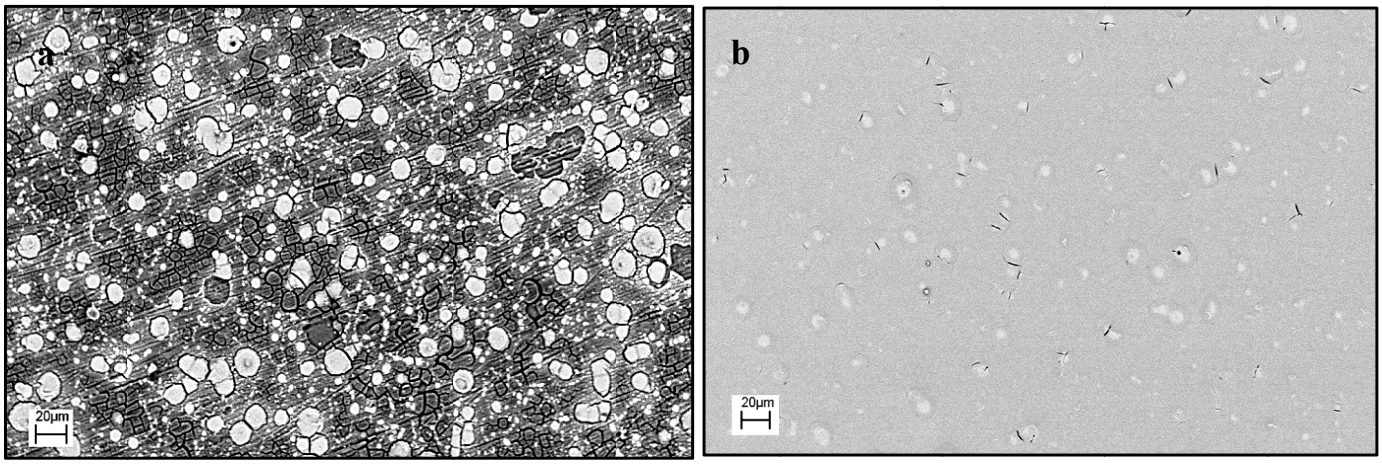

Fig. 1. Surface morphology of the Ti-Zr (a) and Ti-Zr/sol-gel (b) layers

pretreated sample was entirely covered, by the crack-free hybrid sol-gel film. In other words, the applied sol-gel film was spread over the whole cracks of the Ti-Zr layer and entirely covered the surface. However, some micro-defects are observable on the surface of the silica film which is related to the hydrogen gas evolution due to the reaction of magnesium with acidic sol solution or removal of water during the curing process [18,25].

3.2. Electroless Ni-P coating

Fig. 2 represents the surface morphology of Ni-P coating on Ti-Zr and Ti-Zr/sol-gel pretreatment layers after 3 h plating. As the low-magnification images revealed (Fig. 2a and c), the applied Ni-P coating was entirely covered the surface of both pretreated samples and had a cauliflower-like structure. However, a comparison of the electroless coatings revealed that Ni-P coating on the Ti-Zr conversion layer has a more uniform size distribution of the nodules than the applied coating on the Ti-Zr/sol-gel layer. The high magnification image of Ni-P coating on the Ti-Zr layer (Fig. 2b) shows some pits or defects, but the applied coating on the Ti-Zr/sol-gel pretreatment layer (Fig. 2d) has more compact grain boundaries and there were no pits or defects on the surface. Some defects and different size distributions of the electroless coating on these two different pretreatment layers could be attributed to the various formation mechanisms.

The formation mechanism of Ni-P coating on Ti-Zr conversion layer could be presented as follows:

After immersing the sample with the Ti-Zr treated layer into the electroless plating bath, the first nickel nuclei form via the substitution reaction between Mg substrate and Ni ions of the bath through the cracks of the conversion layer. Then, the reduction of nickel continues by the hypophosphite (reaction 9) until the surface covers completely [28].

$$Ni^{2+} + 4H_2PO_2^- + H_2O \rightarrow Ni + \\ + 3H_2PO_3^- + P + H^+ + \frac{3}{2}H_2 \qquad (9)$$

In the case of the electroless coating on Ti-Zr/sol-gel layer, the sol-gel surface is non-catalytic. Moreover, the sol-gel film covers the cracks of the conversion layer and the first nucleation centers could not be formed through the substitution reaction. As was mentioned in the experimental section, the sol-gel film was sensitized and then activated before the electroless plating using $SnCl_2$/HCl and $AgNO_3$/NaOH/NH_3 solutions, respectively. By immersing the Ti-Zr/sol-gel treated sample in the acidic $SnCl_2$ solution, Sn^{2+} ions adsorb on the surface. Then, the sensitized sample was transferred into the activation bath containing $[Ag(NH_3)_2]^+$ ions. The adsorbed Sn^{2+} ions cause the reduction of $[Ag(NH_3)_2]^+$ to Ag as the following reaction [29,30]:

$$2[Ag(NH_3)_2]^+ + Sn^{2+} \rightarrow 2Ag^\circ + Sn^{4+} + 4NH_3 \qquad (10)$$

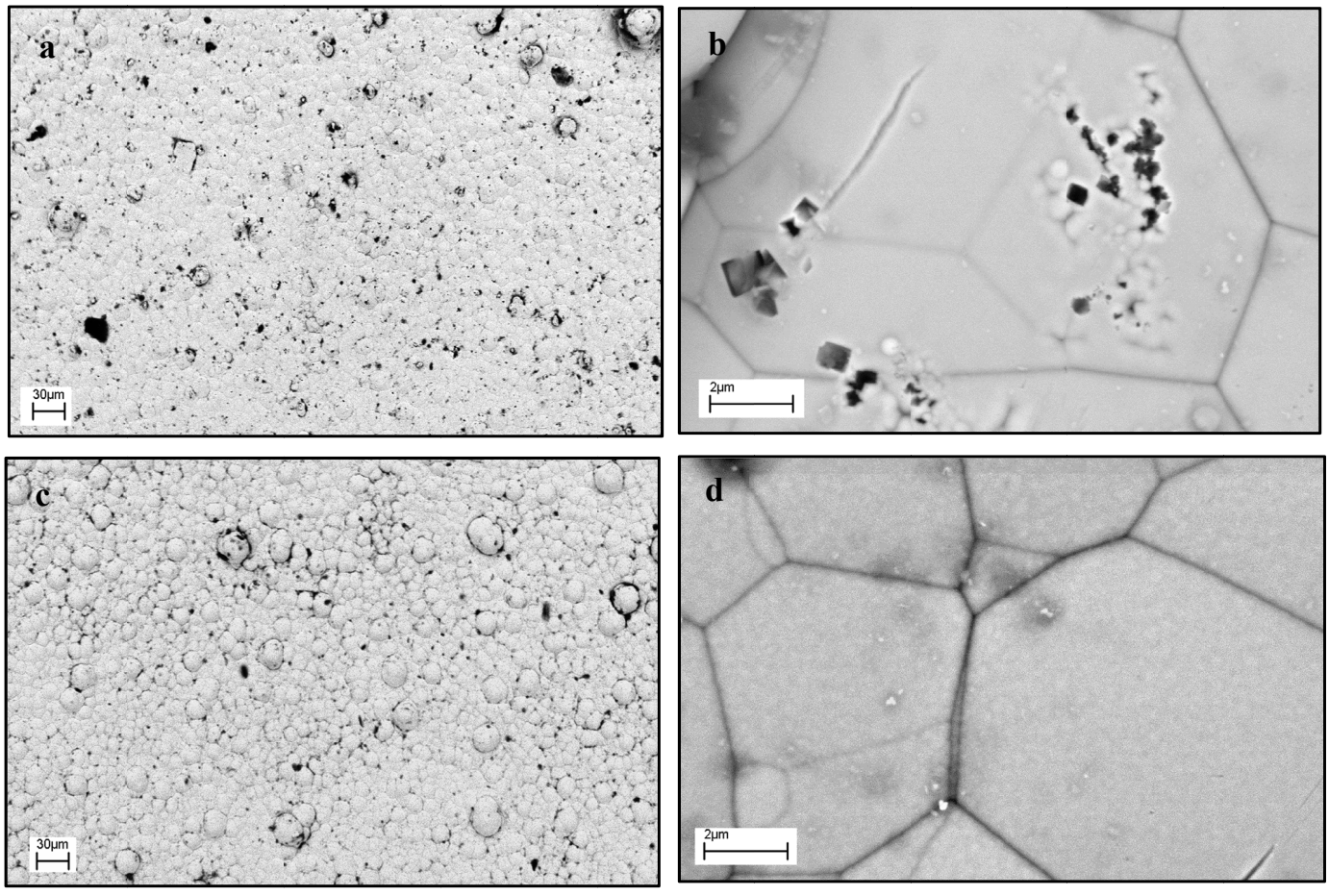

Fig. 2. Surface morphology of the electrolss nickel coating on the Ti-Zr (a and b) and Ti-Zr/sol-gel layer (c and d)

The deposited Ag° particles act as catalytic sites and cause the reduction of Ni^{2+} ions of the plating bath to Ni atoms and so, the initial nuclei forms. The deposited Ni atoms act as a self-catalyst for the further deposition of the coating. The cross-sectional images of both electroless coatings were shown in Fig. 3 after 3 h plating. Both images show no defect or detachment in the interface of substrate-coating. Moreover, the thickness of Ni-P coating on the Ti-Zr conversion layer was 18 µm while in the case of the Ni-P coating on the Ti-Zr/sol-gel pretreatment layer was reached 32 µm. This increase in the thickness was attributed to the different nucleation mechanisms during the electroless plating procedure which was mentioned above in details. In other words, the number of nucleation centers in Ni-P on the Ti-Zr/sol-gel electroless coating is more than the other one and so, the deposition rate is high. More number of nucleation centers leads to more deposition and so increasing in thickness.

The EDS analysis demonstrates that Ni-P coating on Ti-Zr layer containing P (8.61 ±0.92 wt. %), Ni (90.60 ±0.75 wt.%), and Cu (0.80 ±0.17 wt.%). Also, the EDS analysis of Ni-P coating on the Ti-Zr/sol-gel layer shows P, Ni and Cu with the weight percent of 8.63 ±0.31, 90.88 ±0.32, and 0.49 ±0.21, respectively. The results show that both coatings have medium P content and so, the mixed crystalline-amorphous structure. Furthermore, the addition of $CuSO_4.5H_2O$ to the plating bath causes the presence of Cu in the coatings [31].

The XRD pattern of the electroless Ni-P coating on the Ti-Zr layer (Fig. 4) shows some sharp peaks at approximately 32, 34, 37, 48, 57, 63, 69, and 70 degrees relating to the substrate and an abroad peak at 45° corresponding to Ni(111) [15]. These results are confirmed according to (JCPDS card No.65-3365) for Mg, (JCPDS card No.73-1148) for $Mg_{17}Al_{12}$ phase and (JCPDS card No. 04-0850) for Ni [32,33]. However, the XRD pattern of the applied coating on the Ti-Zr/sol-gel pretreatment layer only shows a peak at 45° for nickel. As is evident after using the Ti-Zr/sol-gel as a pretreatment layer, the peaks of the magnesium alloy substrate disappeared which is due to the high thickness and more compact structure of the applied coating. Moreover, the approximately abroad peak of nickel indicates the mixed crystalline-amorphous nature of both coatings which was previously confirmed by the EDS results.

Fig. 5 shows the 3D AFM images of the electroless coating on the Ti-Zr and Ti-Zr/sol-gel pretreatment layers. The surface

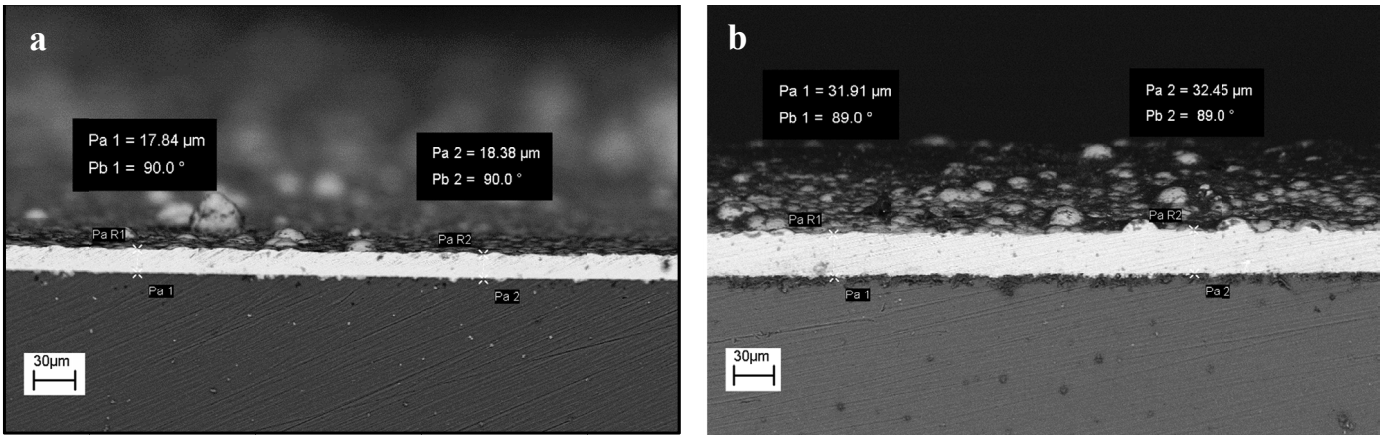

Fig. 3. The cross-sectional view of the electroless Ni-P coating on Ti/Zr (a) and Ti-Zr/sol-gel (b)

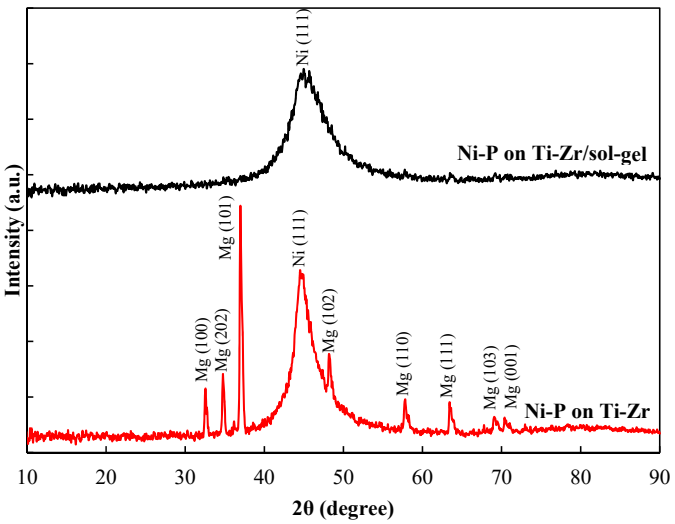

Fig. 4. The XRD pattern of Ni-P coating on Ti-Zr and Ti-Zr/sol-gel pretreatment layer

roughness (R_a) of Ni-P coating on the Ti-Zr and Ti-Zr/sol-gel pretreatment layers was 323 and 718 nm, respectively. As the results show, the surface roughness of the electroless nickel coating on the Ti-Zr/sol-gel layer is high. Probably, this high surface roughness of Ni-P coating on the Ti-Zr/sol-gel layer is as a result of the high deposition rate of the plating process due to a large number of nucleation centers.

3.3. EIS

The EIS response of the electroless nickel coating on the Ti-Zr and Ti-Zr/sol-gel pretreatment layer as Nyquist (a), Bode modulus and phase Bode (b) plots was presented in Fig. 6.

The Nyquist plots of both coatings show only one capacitance semicircle in all measured frequencies which this result was confirmed by the Bode plots, consequently. The existence

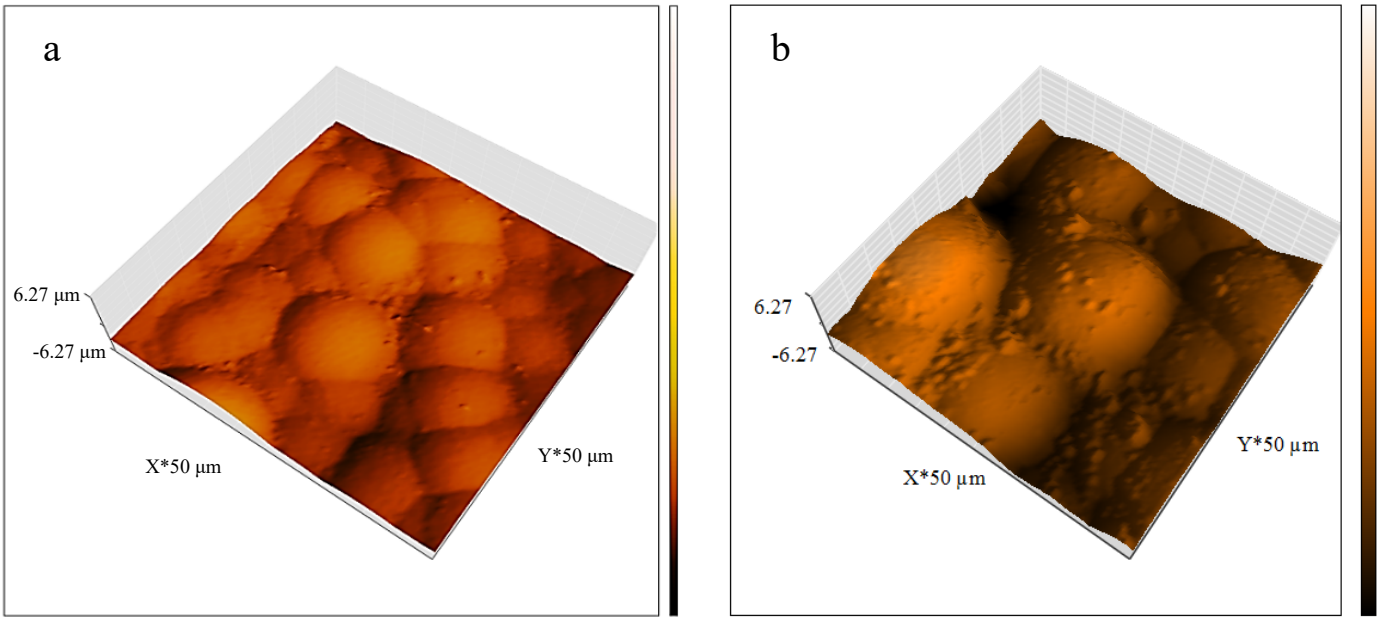

Fig. 5. The AFM image of electroless coating on Ti-Zr (a) and Ti-Zr/sol-gel (b) layer

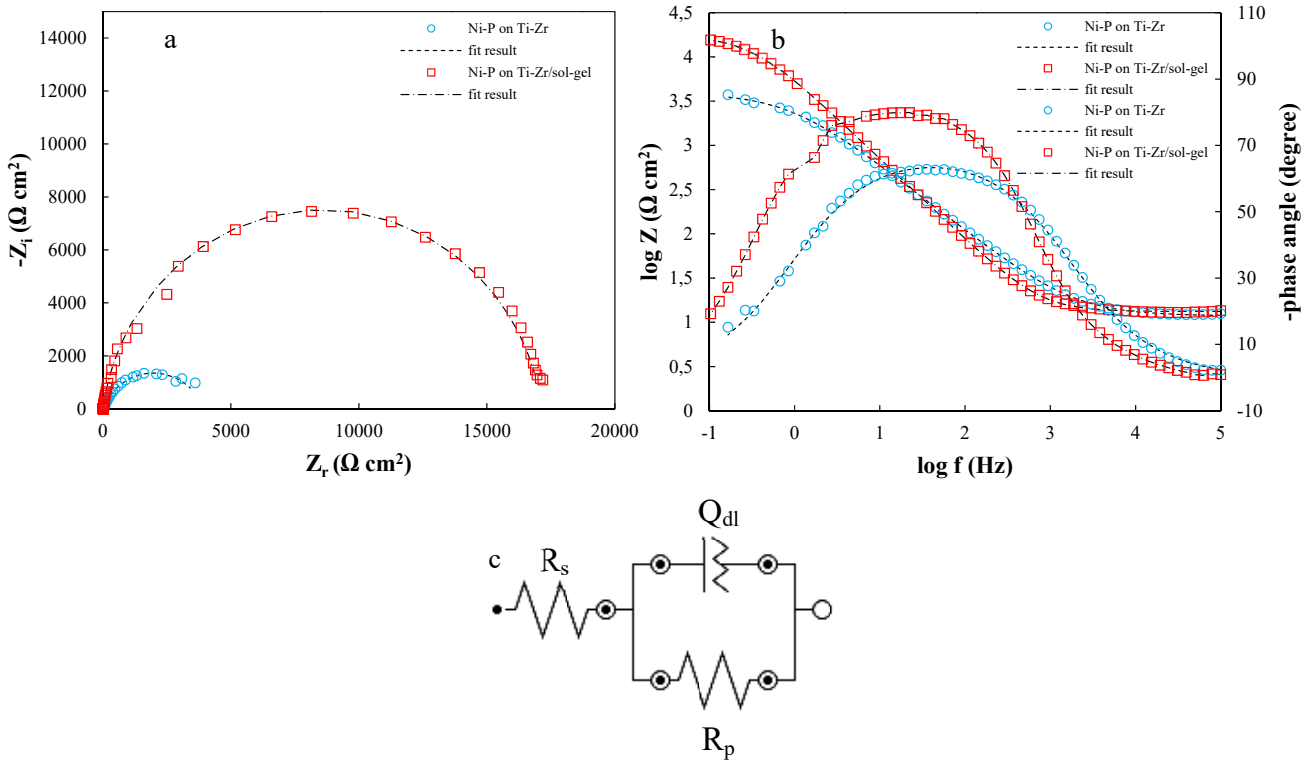

Fig. 6. The EIS plots of electroless coating on Ti-Zr and Ti-Zr/sol-gel pretreatment layer as Nyquist (a), Bode modulus and phase Bode (b)

of one semicircle is associated with the formation of electrical double layer at the interface of coating-corrosive solution and reflects the occurrence of a single electrochemical reaction on the surface of the electrodes. Moreover, a comparison of the Nyquist plots indicates that the diameters of the semicircle for the applied electroless coating on the Ti-Zr/sol-gel pretreatment layer are larger than the other one and this coating has a higher impedance value. The EIS plots of the coatings were fitted using a Randles circuit (Fig. 6c) containing corrosive solution resistance (R_s), Constant Phase Element (CPE_{dl}), and polarization resistance (R_p). In this circuit, CPE_{dl} was inserted instead of pure capacitor non-ideal behavior of electrochemical systems. The impedance of the CPE element is as follows [15]:

$$Z_{CPE} = \frac{1}{Q}(j\omega)^{-n} \tag{11}$$

In this equation, Q represents the constant of the CPE, $j = \sqrt{-1}$, ω is the angular frequency and n is a factor that varies

TABLE 2

Quantitative results of the EIS tests for electroless Ni-P coatings

Sample	Q_{dl} ($\mu s^n\ \Omega^{-1}\ cm^{-2}$)	n	R_p ($k\Omega\ cm^2$)	χ^2	OCP (V)
Ni-P on Ti-Zr	66.76 ±0.70	0.766 ±0.007	3.933 ±0.042	0.0014	–0.348 ±0.18
Ni-P on Ti-Zr/sol-gel	31.60 ±0.19	0.917 ±0.001	17.129 ±0.089	0.0015	–0.432 ±0.033

between 0 and 1 and indicates deviation from the ideal capacitor. The deviation of n away from unity can be attributed to the surface heterogeneity and roughness [9]. The extracting of the experimental data was done by Zview2 software and the relevant results with fitting errors were presented in TABLE 2. The results indicate that the value of R_p for the electroless Ni-P coating on the Ti-Zr pretreatment layer is 3.9 $k\Omega.cm^2$ while it was increased to 17.1 $k\Omega.cm^2$ using the Ti-Zr/sol-gel as the pretreatment layer. The results indicate that the R_p of the electroless coating on the Ti-Zr/sol-gel layer was higher than the applied coating on the Ti-Zr. The low thickness of the electroless coating on the Ti-Zr treated layer and porosity of the coating (which was observable in the SEM image) cause to the penetration of corrosive ions. Therefore, the galvanic effect between magnesium substrate and nickel coating the corrosion resistance. However, the better corrosion protection of the electroless coating on the Ti-Zr/sol-gel pretreated layer is due to the more compact structure. In other words, the corrosion protection performance of the electroless coating in corrosive solution was increased significantly after addition of the sol-gel on the Ti-Zr layer.

3.4. Microhardness

The Vickers microhardness measurements of the electroless coating on the Ti-Zr and Ti-Zr/sol-gel pretreated layers were done. The averaged microhardness value for the applied electroless coating on the Ti-Zr layer was 713 HV while this value was decreased to 560 HV using the Ti-Zr/sol-gel as a pretreatment layer. A comparison of the microhardness value with similar works [35,36] demonstrates that both applied coatings have a suitable microhardness values. Decreasing of the microhardness value for the sample with the Ti-Zr/sol-gel pretreatment layer is probably due to the larger grain size of the applied coating concerning the sample with the Ti-Zr pretreatment layer. Smaller grain size will reduce the dislocation movement in the coating and increase the yield strength which leads to enhancement of hardness.

4. Conclusion

1. The substrate surface was completely covered by the Ti-Zr conversion layer with a cracky structure.
2. The surface of the Ti-Zr conversion layer was completely covered by hybrid sol-gel film.
3. The applied Ni-P coating with a cauliflower-like structure completely covered the surface of both pretreated samples. The size distribution of the nodules in the electroless coating on the Ti-Zr conversion layer was more uniform than the Ti-Zr/sol-gel layer.
4. The thickness of the electroless nickel coating on the Ti-Zr/sol-gel pretreated layer was higher due to more significant number of nucleation centers.
5. The XRD pattern of electroless coating on the Ti-Zr pretreated layer showed the substrate peaks due to low thickness and high penetration deep of the X-ray.
6. The surface roughness of the applied electroless coating on the Ti-Zr/sol-gel layer was higher due to the high deposition rate as a result of large number of nucleation centers.
7. The electroless coating on the Ti-Zr/sol-gel layer has better corrosion protection performance than the coating on the Ti-Zr due to more compact structure.

REFERENCES

[1] G. Duan, L. Yang, S. Liao, C. Zhang, X. Lu, Y. Yang, B. Zhang, Corros. Sci. **135**, 197-206 (2018). DOI: https://doi.org/10.1016/j.corsci.2018.02.051

[2] C. Hu, M. Xu, J. Zhang, B. Hu, G. Yu, J. Alloy. Compd. **770**, 48-57 (2019). DOI: https://doi.org/10.1016/j.jallcom.2018.07.306

[3] X. Liu, W. Sun, Y. Dong, M. Ma, Y. Zhang, F. Yang, Y. Ruan, J. Mater. Res. **34**, 1064-1072 (2019). DOI: https://doi.org/10.1557/jmr.2019.21

[4] A. Mazurek, W. Bartoszek, G. Cieslak, A. Gajewska-Midziałek, D. Oleszak, M. Trzaska, Arch. Metall. Mater. **65**, 839-844 (2020). DOI: https://doi.org/10.24425/amm.2020.132829

[5] A.A. Zuleta, E. Correa, J.G. Castano, F. Echeverria, A. Baron-Wiechec, P. Skeldon, G.E. Thompson, Surf. Coat. Tech. **321**, 309-320 (2017). DOI: https://doi.org/10.1016/j.surfcoat.2017.04.059

[6] D. Seifzadeh, H. Kazemi Mohsenabadi, Z. Rajabalizadeh, RSC Adv. **6**, 97241-97252 (2016). DOI: https://doi.org/10.1039/C6RA19984D

[7] Y. Wei, Y. Li, Y. Zhang, X. Luo, C. Li, Corros. Sci. **138**, 105-115 (2018). DOI: https://doi.org/10.1016/j.corsci.2018.04.018

[8] F. Heakal, M. Shoeib, M. Maanoum, Prot. Met. Phys. Chem. S. **53**, 177-187 (2017). DOI: https://doi.org/10.1134/S2070205116060095

[9] D. Seifzadeh, L. Farhoudi, Surf. Eng. **32**, 348-355 (2016). DOI: https://doi.org/10.1179/1743294415Y.0000000034

[10] P. Zhou, W. Cai, Y. Yang, X. Li, T. Zhang, F. Wang, Surf. Coat. Tech. **374**, 103-115 (2019). DOI: https://doi.org/10.1016/j.surfcoat.2019.05.080

[11] M.R. Majdi, I. Danaee, D. Zaarei, M. Farzam, Arch. Metall. Mater. **65**, 627-638 (2020).
DOI: https://doi.org/10.24425/amm.2020.132802

[12] Z. Gao, D. Zhang, X. Qiu, S. Jiang, Y. Wu, Q. Zhang, X. Li, Corros. Sci. **142** 153-160 (2018).
DOI: https://doi.org/10.1016/j.corsci.2018.07.024

[13] J. Zhang, Z. Song, G. Yu, B. Hu, X. Zhang, Int. J. Electrochem. Sc. **11**, 10053-10066 (2016).
DOI: https://doi.org/10.20964/2016.12.57

[14] D. Seifzadeh, H. Kazemi Mohsenabadi, B. Mater. Sci. **40**, 407-415 (2017).
DOI: https://doi.org/10.1007/s12034-017-1366-4

[15] Z. Rajabalizadeh, D. Seifzadeh, Appl. Surf. Sci. **422**, 696-709 (2017). DOI: https://doi.org/10.1016/j.apsusc.2017.06.100

[16] S. Zhang, Q. Li, J. Fan, W. Kang, W. Hu, X. Yang, Prog. Org. Coat. **66**, 328-335 (2009).
DOI: https://doi.org/10.1016/j.porgcoat.2009.08.011

[17] A.A. El-Hadad, V. Barranco, A. Samaniego, I. Llorente, F.R. Garcia-Galvan, A. Jimenez-Morales, J.C. Galvan, S. Feliu, Prog. Org. Coat. **77**, 1642-1652 (2014).
DOI: https://doi.org/10.1016/j.porgcoat.2014.05.026

[18] N.V. Murillo-Gutierrez, F. Ansart, J.P. Bonino, M.J. Menu, M. Gressier, Surf. Coat. Tech. **232**, 606-615 (2013).
DOI: https://doi.org/10.1016/j.surfcoat.2013.06.036

[19] S. Zhang, Q. Li, B. Chen, X. Yang, Electrochim. Acta. **55**, 870-877 (2010).
DOI: https://doi.org/10.1016/j.electacta.2009.07.053

[20] A.L.K. Tan, A.M. Soutar, I.F. Annergren, Y.N. Liu, Surf. Coat. Tech. **198**, 478-482 (2005).
DOI: https://doi.org/10.1016/j.surfcoat.2004.10.066

[21] Q. Li, B. Chen, S. Xu, H. Gao, L. Zhang, C. Liu, J. Alloy. Compd. **478**, 544-549 (2009).
DOI: https://doi.org/10.1016/j.jallcom.2008.11.123

[22] S. Nezamdoust, D. Seifzadeh, T. Nonferr. Metal. Soc. **27**, 352-362 (2017). DOI: https://doi.org/10.1016/S1003-6326(17)60039-6

[23] N.V. Murillo-Gutierrez, F. Ansart, J.-P. Bonino, M.-J. Menu, M. Gressier, Surf. Coat. Tech. **232**, 606-615 (2013).
DOI: https://doi.org/10.1016/j.surfcoat.2013.06.036

[24] J. Hu, Q. Li, X. Zhong, L. Zhang, B. Chen, Prog. Org. Coat. **66**, 199-205 (2009).
DOI: https://doi.org/10.1016/j.porgcoat.2009.07.003

[25] S. Nezamdoust, D. Seifzadeh, Z. Rajabalizadeh, J. Magnes. Alloy. **7**, 419-432 (2019).
DOI: https://doi.org/10.1016/j.jma.2019.03.004

[26] F. Andreatta, A. Turco, I. De Graeve, H. Terryn, J.H.W. De Wit, L. Fedrizzi, Surf. Coat. Tech. **201**, 7668-7685 (2007).
DOI: https://doi.org/10.1016/j.surfcoat.2007.02.039

[27] A. Yi, J. Du, J. Wang, S. Mu, G. Zhang, W. Li, Surf. Coat. Tech. **276**, 239-247 (2015).
DOI: https://doi.org/10.1016/j.surfcoat.2015.06.069

[28] Y.W. Song, D.Y. Shan, E.H. Han, Electrochim. Acta. **53**, 2135-2143 (2008). DOI: https://doi.org/10.1016/j.electacta.2007.09.026

[29] S. Shukla, S. Seal, Z. Rahaman, K. Scammon, Mater. Lett. **57**, 151-156 (2002).
DOI: https://doi.org/10.1016/S0167-577X(02)00722-X

[30] Z. Aixiang, X. Weihao, X. Jian, Mater. Lett. **59**, 524-528 (2005).
DOI: https://doi.org/10.1016/j.matlet.2004.10.041

[31] Z. Rajabalizadeh, D. Seifzadeh, A. Habibi-Yangjeh, T. Mesri Gundoshmian, S. Nezamdoust, Surf. Coat. Tech. **346**, 29-39 (2018).
DOI: https://doi.org/10.1016/j.surfcoat.2018.04.032

[32] M.J. Balart, Z. Fan, Int. J. Cast Met. Res. **27**, 301-311 (2014).
DOI: https://doi.org/10.1179/1743133614Y.0000000115

[33] S. Ullah Rather, Mater. Res. Bull. **60**, 556-561 (2014).
DOI: https://doi.org/10.1016/j.materresbull.2014.09.027

[34] L. Yang, J. Li, Y. Zheng, W. Jiang, M. Zhang, J. Alloy. Compd. **467**, 562-566 (2009).
DOI: https://doi.org/10.1016/j.jallcom.2007.12.041

[35] W.X. Zhang, J.G. He, Z.H. Jiang, Q. Jiang, J.S. Lian, Surf. Coat. Tech. **201**, 4594-4600 (2007).
DOI: https://doi.org/10.1016/j.surfcoat.2006.09.312